Ultrasonic Phased Array Sparse TFM Imaging Based on Virtual Source and Phase Coherent Weighting

JIN YANG[ID], **LIN LUO, KAI YANG**[ID], **AND YU ZHANG**

School of Physical Science and Technology, Southwest Jiaotong University, Chengdu 610031, China

Corresponding author: Kai Yang (yangkai_swjtu@163.com)

ABSTRACT Total focus method (TFM) is an ultrasonic phased array imaging method and has a larger dynamic focusing range and higher spatial resolution than traditional imaging methods. But TFM needs to process a large amount of data, resulting in a long imaging time, which greatly limits its application and development in the industrial field. The sparse method can improve the computing efficiency by reducing the amount of data, but the resolution and intensity of sparse image are very low. This paper proposes a virtual source sparse TFM (VSSTFM) method based on phase coherent weighting (PCW) to improve the spatial resolution and intensity of the sparse TFM imaging. The layout of virtual sources in the virtual source array is designed and optimized by genetic algorithm. According to the phase distribution characteristics of the ultrasonic testing signal, a phase coherence factor is constructed to weight the VSSTFM image to further improve the image quality. Experimental results show that compared with conventional TFM, the proposed method can improve the imaging efficiency by 66.56 % while providing significantly higher image quality than TFM imaging.

INDEX TERMS Ultrasonic phased array, sparse TFM, virtual source, phase coherent weighting.

I. INTRODUCTION

Compared with traditional ultrasonic testing, ultrasonic phased array testing has higher resolution and sensitivity, and adapts to various complex scenes, which makes it widely used in the nondestructive testing and has a bright prospect [1], [2]. Holmes et al. [3] first proposed the full matrix capture (FMC) and total focusing method (TFM) model in 2005. Compared with traditional phased array imaging, TFM uses a full matrix data, which can focus on any point of the imaging area and has excellent imaging quality. It has been gradually applied to many industrial fields, such as aerospace, nuclear industry, oil and gas, etc. [4]–[6]. Nevertheless, the data of TFM is very large, and the imaging time is very long and cannot be imaged in real time, which limits its further development and application [7].

In order to solve this problem, GPU and FPGA can be used for parallel calculations to reduce the computing time from the perspective of improving the hardware level [8]–[10]. In addition, the imaging efficiency can also be improved by optimizing the TFM algorithm itself. Because FMC data has a certain degree of redundancy [11], the sparse method can be used to reduce the amount of data and computing time, which can greatly improve the imaging speed. Peng et al. [12] reduce the computation time by increasing the array aperture on the basis of the uniform sparse array, but the sound field characteristics of the uniform sparse array are quite different from the full array, and the image is greatly affected by the beam sidelobes. In the optimization method of sparse array, Zhang et al. [13] used the cross-correlation method to reconstruct the Green's function, restored the ultrasonic signal submerged by noise in the near-field area, and optimized the sparse array using genetic algorithm (GA) to achieve sparse TFM imaging of near-surface defects in the plate structure. Hu et al. [14] established a two-layer TFM imaging model, then used GA to optimize the sparse array and used the effective aperture theory to optimize the sparse image. More research results show that GA can effectively optimize the sparse array layout, and the optimized sparse array has better imaging effects.

The associate editor coordinating the review of this manuscript and approving it for publication was Yuhao Liu.

Although the sparse method can improve the comput-ing efficiency, it will cause the image intensity and spatial resolution to decrease. To improve image resolution and reduce the artifacts, Laroche N *et al.* [15] proposed a fast inverse method for deconvolution of TFM images using spa-tially varying point spread function (PSF) to obtain higher-resolution reconstructed images during the iterative process of sparsity and spatial smoothness. The important factors affecting the imaging quality of the phased array are the main-lobe and side-lobe of the array sound field, which must be constrained and optimized by appropriate methods. Zhang H *et al.* [16] fully considered the influence of the main lobe and side lobes of the sound beam on the sound field and used binary particle swarm optimization (BPSO) to sparse the phased array, which improved the imaging efficiency and made the sparse image quality close to full array at the same time. JCE de Souza *et al.* [17] used the array radiation pattern to analyze the influence of the main-lobe and side-lobe levels in the sound field on the sparse results, and the optimized sparse array has a closer imaging resolution and less artifacts than the full array. Zhang *et al.* [18] used instantaneous phase coherence factor (IPCF) and instantaneous phase weighting factor (IPWF) to weight Green's function, which reduces the background noise in the ultrasonic scattering sound field and increases the continuity of the image phase, but the imaging time has not been reduced compared with conventional TFM. On the whole, better image quality often requires longer imaging time, and the high computational efficiency of sparse TFM is usually at the expense of reduced resolution and image intensity.

To solve this problem, this paper proposes a virtual source sparse TFM (VSSTFM) method based on phase coherent weighting (PCW). First, according to the directivity of the sound beam, the influence of side-lobe and main-lobe on the sound field radiated by the array are considered com-prehensively. The sparse array is designed and optimized by GA, and the beam directivity of the obtained sparse array is similar to full array. Second, a VSSTFM imaging model is established to improve the imaging resolution and suppress the background noise in sparse image. The virtual source array is composed of multiple virtual sources, and the position of each virtual source is determined by the layout of real sparse phased array. Third, according to the phase distri-bution characteristics of the defect signal and noise signal in the ultrasonic testing signal, a phase coherence factor is constructed to weight the VSSTFM image. This method can weaken the signal of other imaging areas while enhancing the defect information, and eliminate the artifacts around the defect. Finally, a specimen with circularly distributed artificial defects is used for the experiment. The three indexes of array performance index (API), SNR, and computing time are used to quantitatively analyze the imaging quality and imaging efficiency.

The paper is organized as follows: Section I introduces the research background and main content of the paper. Section II introduces the theory of VSSTFM and PCW and the results
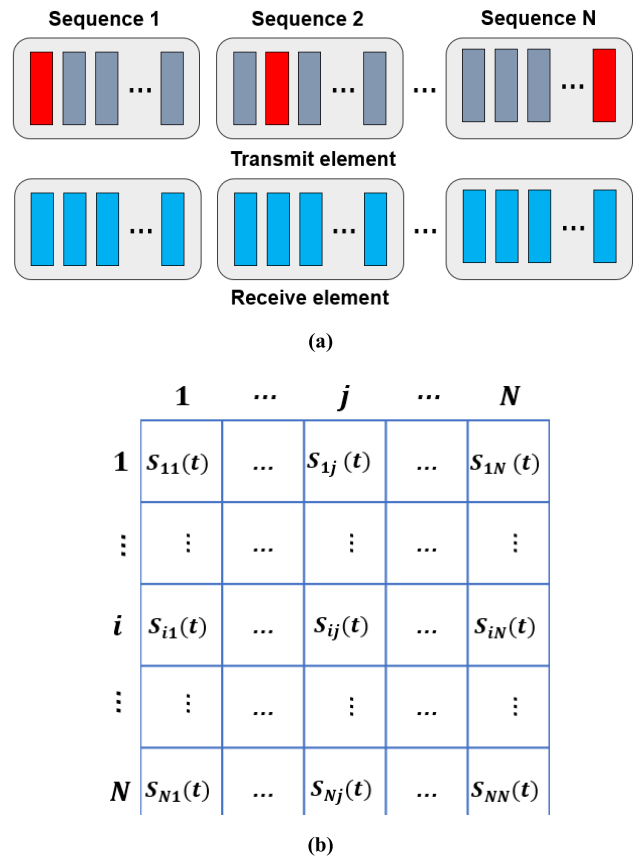

FIGURE 1. The schematic diagram of FMC. (a) Signal acquisition process; (b) Full matrix data.

of sparse array optimized by GA. Section III shows the content and results of the experiment. Section IV analyzes and discusses the experimental results. Section V concludes the paper.

II. THEORY

A. VIRTUAL SOURCE SPARSE TFM

TFM is an ultrasonic phased array imaging method based on full matrix capture (FMC) data. The process of FMC is shown in Fig. 1(a), a linear array excites each element in turn, and then uses all elements to receive the echo signal. As shown in Fig. 1(b), when the *i-th* element is excited, the echo signal received by the *j-th* element is denoted as $S_{ij}(t)$, where $i = 1, 2, \ldots, N, j = 1, 2, \ldots, N$. After all elements are excited, $N * N$ sets of full matrix data are obtained.

The TFM imaging model is established as shown in Fig. 2. Above the imaging model is a linear ultrasonic transducer array with N elements, and below the transducer array is the imaging area. The origin of the XOZ coordinate system is set to the center of the array, the X-axis is along the array direction, and the Z-axis is perpendicular to the transducer array.

According to the principle of wave superposition, the sig-nal intensity at $P(x, z)$ in the imaging area can be expressed
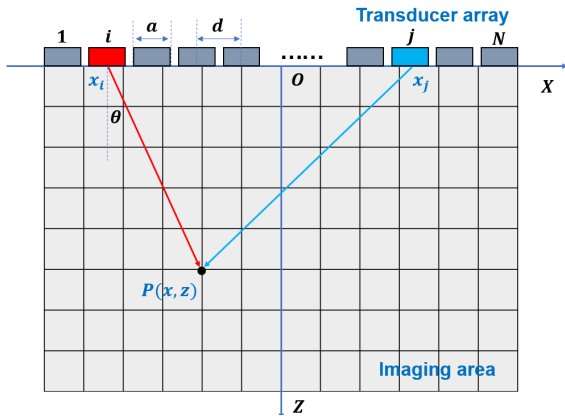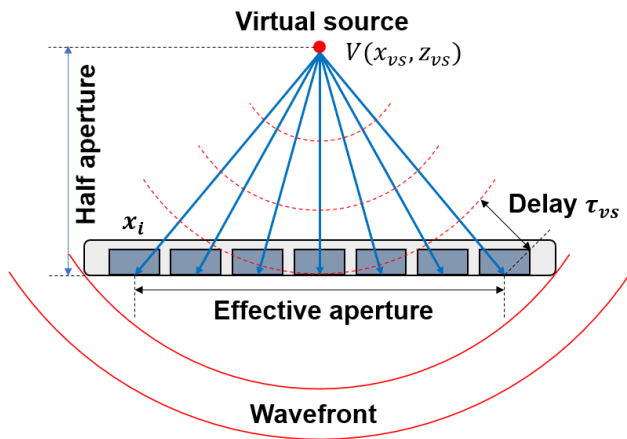
FIGURE 2. The schematic diagram of TFM.

FIGURE 3. Single virtual source model above the real array.

as:

$$I(x, z) = \sum_{i=1}^{N} \sum_{j=1}^{N} S_{ij}(t)$$
$$= \sum_{i=1}^{N} \sum_{j=1}^{N} S_{ij} \left(\frac{\sqrt{(x-x_i)^2 + z^2} + \sqrt{(x-x_j)^2 + z^2}}{c} \right),$$
(1)

where S_{ij} is the intensity of the imaging point $P(x, z)$ in the signal transmitted by the i-th element and received by the j-th element, x_i and x_j denote the coordinates of the excitation and receiving elements, respectively, and c is the speed of ultrasound in the specimen.

As shown in Fig. 3, a virtual sound source is placed above the real array, and the vertical distance from the array is half of the effective aperture of ultrasonic transducer. The spherical wavefront generated in the area below the array by single virtual source can be regarded as the spherical wavefront generated by the entire sparse array [19].

Although there is no real ultrasonic energy source at the position of the virtual source, the virtual source can be simulated by applying a reasonable delay to every element in real
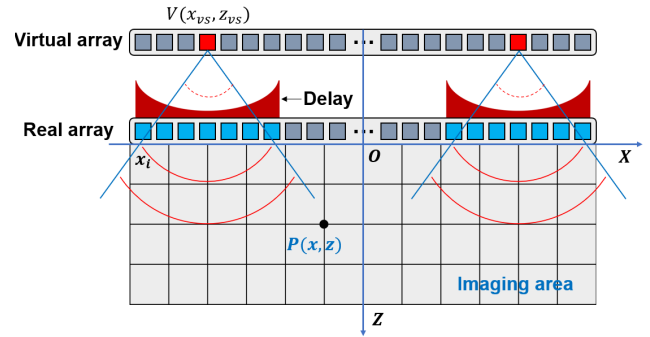
array. The delay τ_{vs} between the transmitting element i $(x_i, 0)$ and virtual source $V(x_{vs}, z_{vs})$ can be calculated as

$$\tau_{vs} = \frac{\sqrt{(x_i - x_{vs})^2 + z_{vs}^2} - z_{vs}}{c}.$$
(2)

Multiple virtual sources are combined into a virtual source array, and the VSSTFM imaging model is established as shown in Fig. 4, where the position of each virtual source is determined by the layout of the real sparse array.

The intensities of all virtual sources in the virtual source array are superimposed, and the VSSTFM image intensity at imaging point $P(x, z)$ is

$$I_{VSSTFM}(x, z) = \sum_{v=1}^{V} I_v(x, z) = \sum_{v=1}^{V} \sum_{i=1}^{m} \sum_{j=1}^{m} S_{ij}(t'), \quad (3)$$

where V is the number of virtual sources, $I_v(x, z)$ is the intensity of the v-th virtual source at point $P(x, z)$, and m is the number of elements in the real phased array that constitutes the v-th virtual source. When $m = 7$, the synthesized sound field of the real array is closest to the sound field of single virtual source [20]. $S_{ij}(t')$ is the virtual source signal obtained by adding a delay τ_{vs} to the echo signal $S_{ij}(t)$, where

$$t' = \frac{\sqrt{(x-x_i)^2 + z^2} + \sqrt{(x-x_j)^2 + z^2} + \sqrt{(x_i - x_{vs})^2 + z_{vs}^2} - z_{vs}}{c}.$$
(4)

B. SPARSE ARRAYS OPTIMIZATION

The array layout will directly affect the imaging quality. GA is a method to find the optimal solution within a certain range [21], which can be used to design and optimize the element position of the sparse array.

GA performs population initialization and randomly generate a chromosome containing N genes firstly. The chromosome and the gene respectively represent the population and the individual, and the individual is encoded with binary digits 0 and 1. The optimization goal of GA is to obtain an optimal element coordinate vector $I = [i_1, i_2, \ldots, i_N]$, which minimizes the peak side-lobe (PSL) and main-lobe width (MLW) of the sparse array [22]. The sound field intensity of

FIGURE 4. The imaging model of VSSTFM.

element i at point $P(x, z)$ is [23].

$$I_i(r, \theta, t) = (\frac{i_0}{r})^{1/2} \frac{\sin(2\pi/\lambda \cdot a \sin \theta / 2)}{2\pi/\lambda \cdot \sin \theta / 2} \exp(-\frac{j\pi a \sin \theta}{\lambda})$$
$$\times \exp[j(2\pi f t - \frac{2\pi r}{\lambda})], \quad (5)$$

where

$$r = \sqrt{(x - x_i)^2 + z^2}, \quad (6)$$

θ is the deflection angle, λ is the wavelength, f is the excitation frequency of transducer, a is the element width.

The synthesized sound field intensity $I(r, \theta, t)$ of a N-element phased array is

$$I(r, \theta, t) = \sum_{i=1}^{N} \varphi_i I_i(r, \theta, t), \quad (7)$$

where $\varphi_i = 1$ means the element i is active, $\varphi_i = 0$ means the element i is not active.

The beam directivity function D_θ of a phased array is

$$D_\theta = \left| \frac{I(r, \theta, t)}{I(r, 0, t)} \right|. \quad (8)$$

Then the PSL and MLW of a phased array can be obtained according to the function D_θ. Considering the goal of sparse optimization, the fitness function of GA is defined as

$$Fitness\,[i_1, i_2, \ldots, i_N] = \min\{\delta_1 * PSL\,[i_1, i_2, \ldots, i_N]$$
$$+ \delta_2 * MLW\,[i_1, i_2, \ldots, i_N]\}, \quad (9)$$

where δ_1 and δ_2 are weight value. Considering both PSL and MLW, the value of δ_1 and δ_2 are set to 1.

The traditional genetic operator will produce individuals who do not meet the constraints, so the modified generalized crossover operator and mutation operator are used for calculation. This operator acts on a matrix containing all individual genes, which can complete the recombination and mutation between individuals to obtain the best individual in the offspring population. Let the parent population be I and the offspring population I', then two parent populations are

$$\begin{cases} I_1 = (i_{1,1}, i_{2,1}, \ldots, i_{N-1,1}, i_{N,1}) \\ I_2 = (i_{1,2}, i_{2,2}, \ldots, i_{N-1,2}, i_{N,2}). \end{cases} \quad (10)$$

Set the crossover probability to p_c. For two randomly selected parent populations, each individual in the population generates a random number on the interval [0, 1]. If $r_i < p_c$, the i-th individual is used for the crossover operation. Crossover operation is to exchange some genes on two chromosomes to form a new chromosome. For example, crossover operation is performed on the first three genes of chromosomes 1100001 and 1010101, and the two new chromosomes obtained are 1010001 and 1100101 respectively. The crossover operation can improve the search ability of genetic algorithm. After the operation of the generalized crossover operator, the offspring populations are

$$\begin{cases} I_1' = Crossover\,(i_{1,1}, i_{2,1}, \ldots, i_{N-1,1}, i_{N,1}) \\ I_2' = Crossover\,(i_{1,2}, i_{2,2}, \ldots, i_{N-1,2}, i_{N,2}). \end{cases} \quad (11)$$

TABLE 1. The parameters set in GA.

Parameter	Value
Number of elements	32
Transducer center frequency	5 MHz
Element width	0.5 mm
Element pitch	0.6 mm
Speed of sound	5900 m/s
Initial population	40
Number of iterations	400
Crossover probability	0.5
Mutation probability	0.01

The purpose of mutation operation is to make gene mutation, prevent the algorithm from falling into local optimum and help the algorithm find the global optimal solution. Set a mutation probability p_m. For the chromosome after the crossover operation, each gene on the chromosome generates a random number r_i in the interval [0, 1]. If $r_i < p_m$, the gene mutates. For a binary coded chromosome, the mutation operation is to change gene 1 to 0 or change gene 0 to 1. For example, if the third gene of chromosome 1100001 is mutated, the new chromosome is 1110001. Repeat this process continuously and record the chromosome structure obtained in each cycle. When the number of iterations reaches the preset value, the chromosome structure with the highest fitness is the best sparse array optimized by GA.

The value range of the initial population is generally 20 $\sim$200. When the initial population is large, the results of GA cannot be optimized, but it will prolong the convergence time and waste resources. The value range of the number of iterations is generally 100$\sim$1000. When the number of iterations is small, the algorithm is not easy to converge. When the number of iterations is large, the algorithm has already converged, and it is meaningless to continue the iteration. According to some experimental results and experience, the relevant parameters set in GA are shown in Table 1.

The directivity diagrams of 32-element phased array is shown in Fig. 5(a), where PSL is -14.6 dB and MLW is 7.2°. Take for example when the number of active element is 8, the directivity diagrams of uniform sparse array is shown in Fig. 5(b), where PSL is -15.3 dB and MLW is 12.6°. Compared with the full array, PSL dropped by 0.7 dB and MLW increased by 75 %. Using GA to optimize the sparse array, the directivity diagrams is shown in Fig. 5(c), where PSL is -19.2 dB and MLW is 8°. Compared with the full array, PSL dropped by 4.6 dB and MLW increased by 11 %. The comparison results show that the sparse array optimized by GA has smaller PSL and MLW, and its imaging characteristics are closer to full array.

GA is used to sparse the 32-element linear phased array with different degrees, and the results are shown in Table 2. The distribution of active elements in the sparse array determines the position of each virtual source in the virtual source array. For example, when
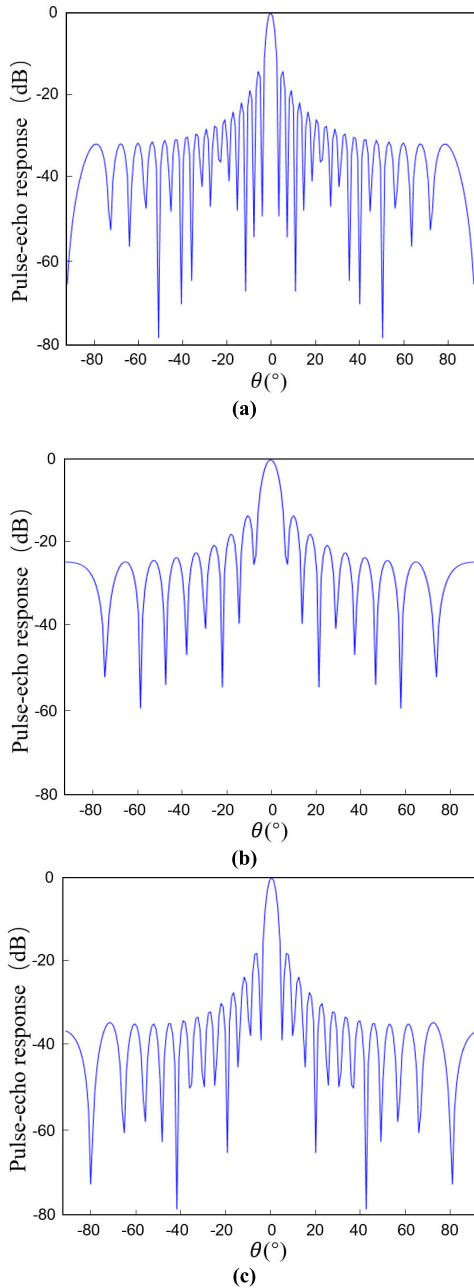
FIGURE 5. The directivity diagram of different phased arrays. (a) 32-element; (b) 8-element uniform sparse array; (c) 8-element sparse array optimized by GA.

TABLE 2. The layout of sparse array optimized by GA.

Active Elements	Array Layout
16	1010001110000111101011010100110001
12	1000100000011010100101100100000011
8	1000000101000000110010000010000001
6	1000000000010000110000000010000001
4	1000000000000100100000000000000001
2	0000000000010000010000000000000000

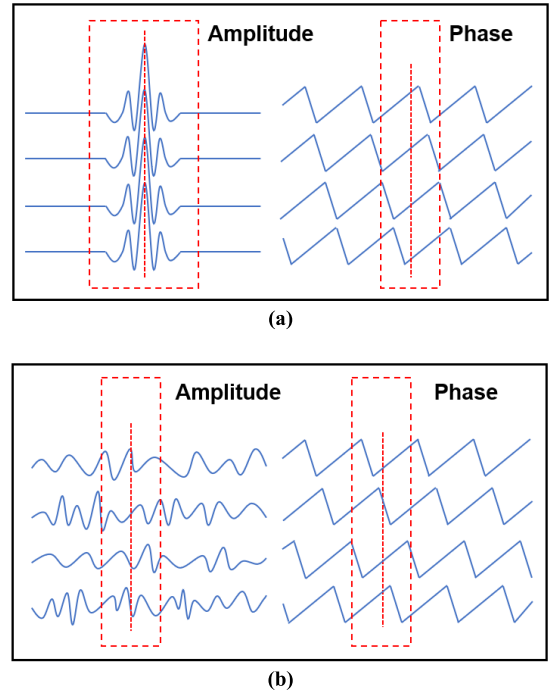**FIGURE 6.** Amplitude and phase distribution of defect signal and noise signal in ultrasonic A-scan. (a) Defect signal; (b) Noise signal.

the number of active elements is 4, the virtual source array layout is 1000000000000100100000000000000001, and the actual array layout used for VSSTFM imaging is 1111000001111111110000000001111.

C. PHASE COHERENCE WEIGHTING

The wavefront generated in the area below the array by a single virtual source is only approximate to the synthesized wavefront of the real array rather than completely consistent, which will increase the PSL and MLW of the array and generate artifacts. As shown in Fig. 6, in the ultrasonic A-scan, the signal at the defect has a higher amplitude and better phase consistency than the noise signal. Based on this, the phase coherent weighting (PCW) is used to enhance the image globally. PCW is an adaptive weighting method, which needs construct a phase coherence factor based on the phase distribution characteristics of ultrasonic testing signal.

The phase coherence factor is used to weight the amplitude-superimposed image to reduce noise, remove artifacts, and highlight defect information.

Using Euler's formula to extract the phase information of signal $S_{ij}(t)$

$$H\left[S_{ij}(t)\right] = |h| e^{j\varphi_{ij}} = |h|\left(\cos\varphi_{ij} + j\sin\varphi_{ij}\right), \quad (12)$$

where H is Hilbert transform, $|h|$ and φ_{ij} are the modulus and phase of the signal respectively. If the modulus of the signal is ignored, the complex random variable Y is

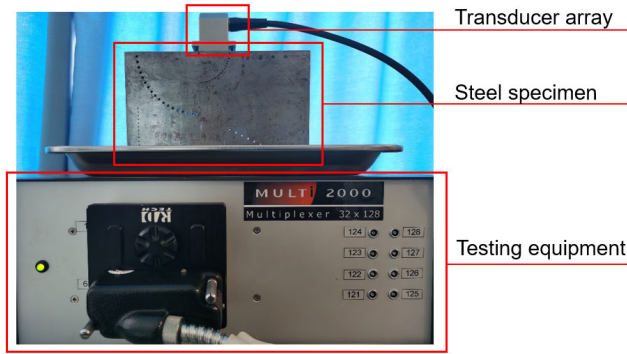$$Y = e^{j\varphi_{ij}} = \cos\varphi_{ij} + j\sin\varphi_{ij}. \quad (13)$$

FIGURE 7. Diagram of the experiment platform.

TABLE 3. Experimental parameters.

Parameter	Value
Data acquisition equipment	Multi2000, M2M(France)
Transducer array	5L32, Olympus(Japan)
Number of elements	32
Element width	0.5 mm
Element pitch	0.6 mm
Transducer center frequency	5 MHz
Sampling frequency	100 MHz
Bandwidth	50 %
Material speed of sound	5900 m/s
Computer configuration	CPU:i5-8300H; RAM:16 GB

Taking phase as an independent variable, the variance of Y is

$$var(Y) = E\left[(Y - \beta)(Y - \beta)^*\right], \quad (14)$$

where β is the average value of Y, and $(Y - \beta)^*$ is the conjugate of $(Y - \beta)$, then the standard deviation of Y is

$$std(Y) = \sqrt{var(Y)} = \sqrt{var(\cos \varphi_{ij}) + var(\sin \varphi_{ij})}. \quad (15)$$

After normalization, the range of $std(Y)$ is [0, 1], when φ_{ij} distribute uniformly in the range $[-\pi, \pi]$, $std(Y) = 1$, and when φ_{ij} are equal, $std(Y) = 0$. The phase coherence factor $F_{PCW}(x, z)$ can be defined using the phase standard deviation $std(Y)$

$$F_{PCW}(x, z) = 1 - \sqrt{var(\cos \varphi_{ij}(x, z)) + var(\sin \varphi_{ij}(x, z))}, \quad (16)$$

where

$$var(\cos \varphi_{ij}(x, z)) = \frac{1}{N^2} \sum_{i=1}^{N} \sum_{j=1}^{N} \cos^2 \varphi_{ij}$$

$$- \left(\frac{1}{N^2} \sum_{i=1}^{N} \sum_{j=1}^{N} \cos \varphi_{ij}\right)^2, \quad (17)$$

$$var(\sin \varphi_{ij}(x, z)) = \frac{1}{N^2} \sum_{i=1}^{N} \sum_{j=1}^{N} \sin^2 \varphi_{ij}$$

$$- \left(\frac{1}{N^2} \sum_{i=1}^{N} \sum_{j=1}^{N} \sin \varphi_{ij}\right)^2. \quad (18)$$

The phase coherence factor can well recognize the defect signal and noise in the ultrasonic A-scan. The phase diversity of defect signal is small, at this time $F_{PCW}(x, z)$ approaches unity. The phase diversity of noise is large, at this time $F_{PCW}(x, z)$ approaches zero. Using $F_{PCW}(x, z)$ to weight the VSSTFM image, the intensity of the PCW-VSSTFM image at the imaging point $P(x, z)$ can be obtained as follows:

$$I_{PCW-VSSTFM}(x, z) = I_{VSSTFM}(x, z) \cdot F_{PCW}(x, z). \quad (19)$$
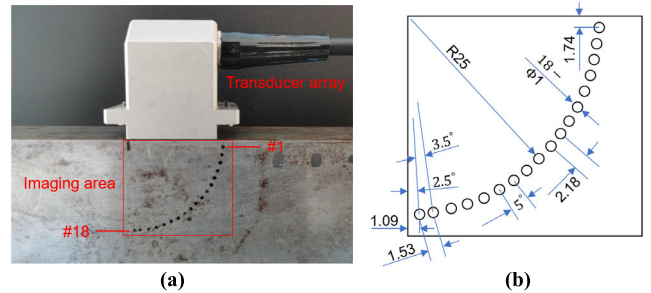

FIGURE 8. The steel specimen in the experiment. (a) Specimen and imaging area; (b) Parameters of the artificial holes.
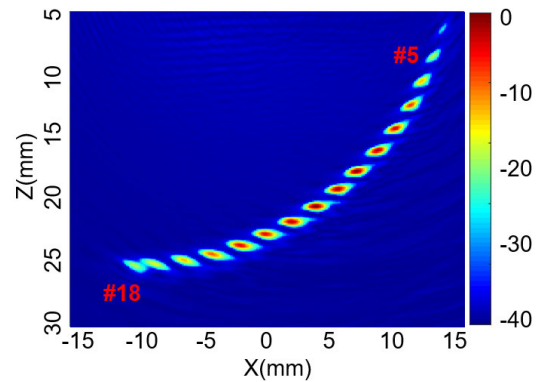

FIGURE 9. The result of 32-element array TFM imaging.

III. EXPERIMENTS AND RESULTS
A. EXPERIMENTS AND EVALUATION INDEX
The portable ultrasonic phased array testing equipment is used to test the steel specimen containing artificial defects, and the ultrasonic signal is acquired for verification of the algorithm. The experiment platform is shown in Fig. 7, which mainly includes a portable ultrasonic phased array flaw detector, an ultrasonic transducer array and a steel specimen. The relevant parameters in the experiment are shown in Table 3.

The steel specimen used in the experiment is shown in Fig. 8(a). The imaging area contains 18 artificial defects with a diameter of 1 mm, which are sequentially numbered #1-#18. The imaging area is 40 mm∗60 mm, and the grid
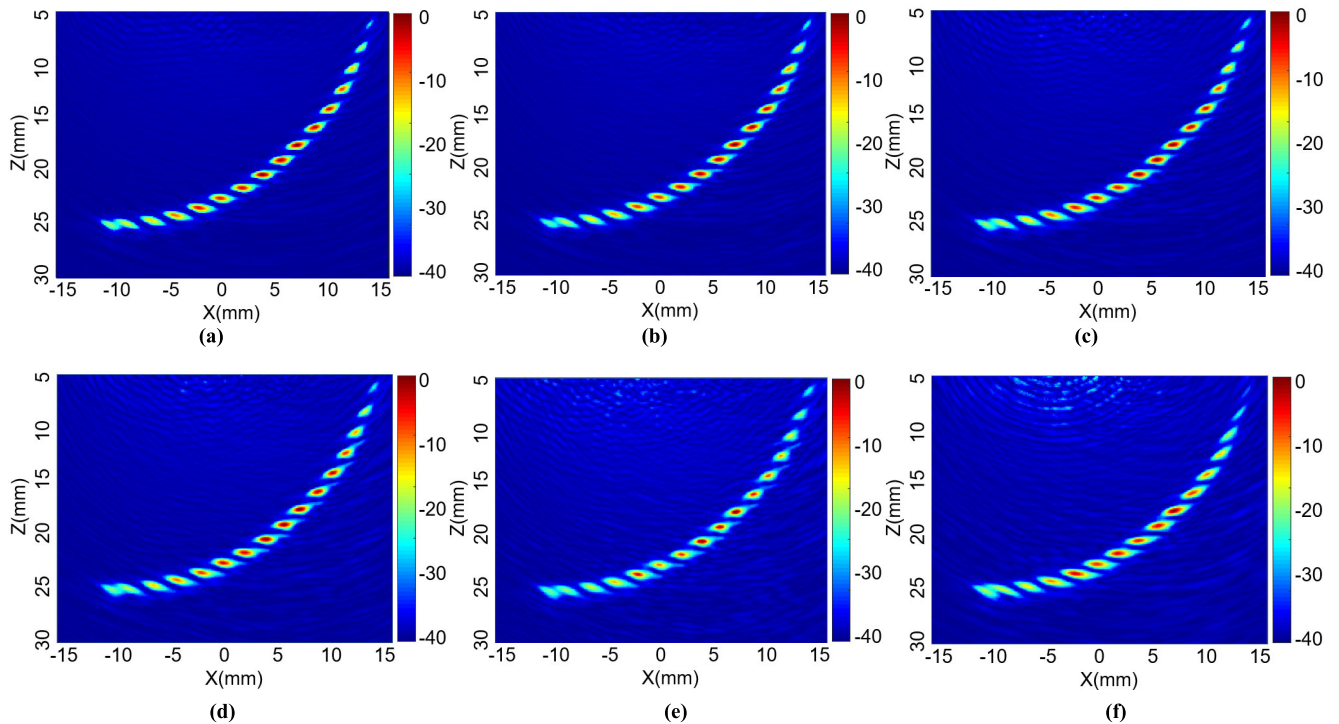
FIGURE 10. The results of sparse TFM with various numbers of active element. (a) 16-element; (b) 12-element; (c) 8-element; (d) 6-element; (e) 4-element; (f) 2-element.

FIGURE 11. Comparison of API and SNR of TFM images with different sparse arrays. (a) API; (b) SNR.

pixels are 400*600. The parameters of the artificial holes in the specimen are shown in Fig. 8(b).

API and SNR are used to quantitatively evaluate the quality of TFM images. API can reflect the spatial imaging resolution of TFM [24]. The smaller the API, the higher the imaging resolution and measurement accuracy. The expression is as follows

$$API = \frac{A_{-6\text{dB}}}{\lambda^2}, \qquad (20)$$

where $A_{-6\text{dB}}$ is the area of the point spread function that is greater than -6 dB down from its maximum value, λ is the wavelength.

SNR reflects the intensity of defect information in the image. The larger the SNR, the better the image quality. The expression is as follows

$$SNR = 20 \cdot \log_{10} \left| \frac{I_{\max}}{I_{average}} \right|, \qquad (21)$$

where $I_{\max}$ is the peak value of the defect signal, and $I_{average}$ is the average intensity of the noise.

B. RESULTS

The result of 32-element array TFM imaging is shown in Fig. 9. The imaging quality of #5-#18 defects in the TFM
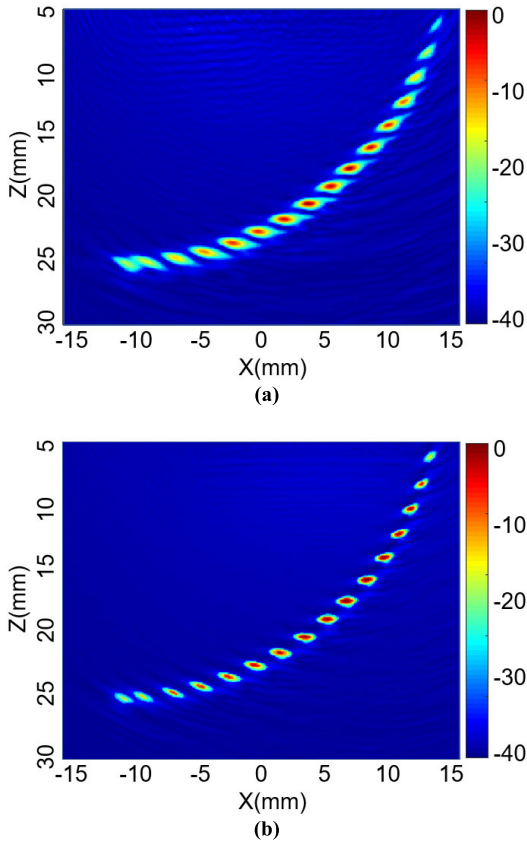
FIGURE 12. The results of sparse TFM imaging with 4-element array. (a) VSSTFM; (b) PCW-VSSTFM.

TABLE 4. The indexes of various sparse TFM images.

Active elements	API	SNR(dB)	TIME(s)
32	0.728	-5.706	19.65
16	0.704	-9.211	10.35
12	0.748	-11.042	7.72
8	0.789	-13.377	5.09
6	0.807	-15.216	4.13
4	0.998	-13.932	2.71
2	1.125	-20.714	1.84

image is good, which can reflect the shape and distribution of the real defects, and have a low background noise level.

The sparse TFM images of sparse arrays with different numbers of active elements are shown in Fig. 10. It can be seen that as the number of active elements in the sparse array decreases, the background noise of the sparse image and the artifacts around the defect gradually increase, and the intensity of defect signal decreases.

Set the SNR of #10 defect with the highest amplitude in 32-element TFM image as 0 dB. The averages of API and SNR of #5-#18 defects in various sparse TFM images are shown in Table 4.

The comparison results of the averages of API and SNR of sparse TFM images are shown in Fig. 11. With the decrease of

active elements, the average API of sparse TFM images gradually increases, and the average SNR gradually decreases. Compared with 32-element TFM image, when the active elements are less than 4, the error of average API of sparse TFM image reaches 82.85 %, and the average SNR decreases by 16.01 dB. The API and SNR of the 4-element sparse TFM image are close to those of the full array, and the computing time is only 2.71 s. Therefore, the 4-element sparse array is selected for the next optimization.

The result of the 4-element sparse TFM image enhanced by the virtual source is shown in Fig. 12(a). Compared with the 4-element sparse TFM image, the background noise of the VSSTFM image is greatly reduced, the resolution and intensity of defects are enhanced, and the overall image quality is greatly improved, but there are artifacts around the defects. The result of VSSTFM image processed by PCW is shown in Fig. 12(b). Compared to VSSTFM image, PCW-VSSTFM image has less noise, higher spatial resolution and defect intensity, and eliminates the artifacts around the defects. Moreover, the imaging resolution and intensity of PCW-VSSTFM exceed the 32-element TFM imaging.

IV. DISCUSSION

The API of #5-#18 defects in imaging results of four methods are shown in Fig. 13. Overall, the API of defects located directly below the center of the transducer in the TFM image are usually low. And the farther the defects are from the center of the transducer, the larger the API. Compared with TFM, the API of sparse TFM images is obviously increased, which shows that the spatial imaging resolution of sparse TFM is greatly reduced. This is mainly caused by the increase of the beam side-lobe and the decrease of the main-lobe width. Compared with sparse TFM, the API of VSSTFM images are greatly reduced, but still higher than TFM. This shows that the virtual source can well improve the intensity of the main-lobe of beam while reducing the PSL, and improve the imaging resolution of the sparse array. But the imaging accuracy still has a gap with TFM. And due to the difference of the sound field between the virtual source and the real array, there are artifacts around the defects in the VSSTFM image. The API of PCW-VSSTFM image is the lowest in several methods, and has the highest imaging resolution and accuracy.

The SNR of #5-#18 defects in imaging results of four methods are shown in Fig. 14. Overall, the SNR of defects located directly below the center of the transducer in TFM images are higher than defects at the edge. TFM performs imaging by superimposing the signal amplitude of the imaging area. The data of sparse TFM is greatly reduced, and the amplitude after superposition at the defect is very low and the noise is strong, resulting in a significant reduction in SNR of the sparse image. The virtual source array can compensate the intensity of the sparse array. The SNR of VSSTFM image is greatly improved compared with sparse TFM, but the overall intensity is still lower than TFM. The SNR of PCW-VSSTFM image is the highest among several methods. Unlike VSSTFM, which directly compensates for
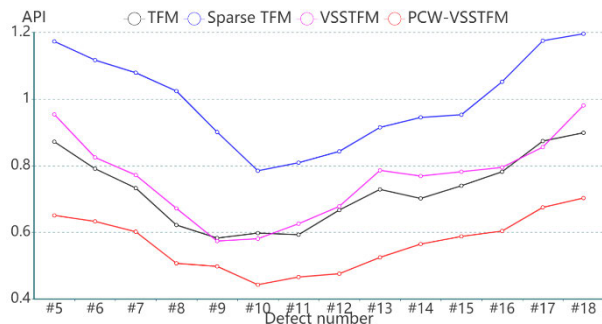
FIGURE 13. Comparison of API of #5-#18 defects in imaging results of four methods.
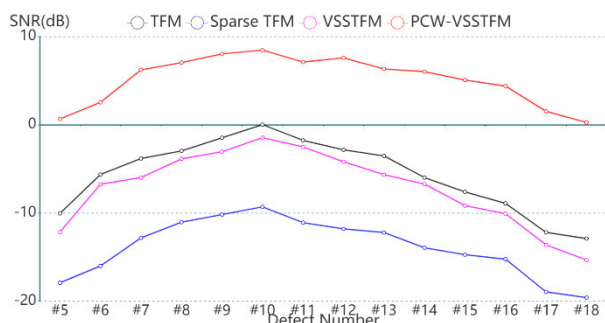

FIGURE 14. Comparison of SNR of #5-#18 defects in imaging results of four methods.

TABLE 5. The averages of API and SNR of imaging results of four methods.

Method	TFM	Sparse TFM	VSSTFM	PCW-VSSTFM
API	0.728	0.998	0.761	0.567
SNR(dB)	-5.706	-13.932	-7.197	5.077
TIME(s)	19.65	2.71	4.83	6.57

the strength of signal, PCW uses a phase coherent factor to weaken the noise to improve SNR, while eliminating the artifacts around the defect and highlighting the defect information.

The averages of API and SNR of #5-#18 defects in imaging results of four methods are shown in Table 5.

Compared with TFM and sparse TFM, the average spatial resolution of PCW-VSSTFM imaging is increased by 22.12 % and 43.19 %, and the average imaging intensity is increased by 10.78 dB and 19.01 dB, respectively. PCW-VSSTFM improves the quality of sparse images very well. Its imaging resolution and intensity are both higher than conventional TFM, and the computing efficiency is increased by 66.56 %.

V. CONCLUSION
The application and development of TFM imaging in industry is limited by the long computing time. Although the traditional sparse method can improve the computing efficiency by reducing the amount of data, the image quality is seriously degraded. This paper proposes a virtual source sparse

TFM (VSSTFM) method based on phase coherent weighting (PCW) to improve the quality of the sparse TFM image. The results show that compared with conventional TFM imaging, the imaging resolution of PCW-VSSTFM is increased by 22.12 %, the imaging intensity is increased by 10.78 dB, and the imaging efficiency is improved by 66.56 %. The proposed method can be used to optimize the phased array, which has certain reference value for the application of TFM real-time imaging in industry. Further, the method will be verified and improved on media with irregular surfaces in the future.

REFERENCES
[1] H. Taheri and A. A. Hassen, "Nondestructive ultrasonic inspection of composite materials: A comparative advantage of phased array ultrasonic," *Appl. Sci.*, vol. 9, no. 8, p. 1628, Apr. 2019.
[2] R. Mohammadkhani, L. Z. Fragonara, P. M. Janardhan, I. Petrunin, A. Tsourdos, and I. Gray, "Ultrasonic phased array imaging technology for the inspection of aerospace composite structures," in *Proc. IEEE 5th Int. Workshop Metrol. Aerosp. (MetroAeroSpace)*, Jun. 2019, pp. 203–208.
[3] C. Holmes, B. Drinkwater, and P. Wilcox, "Post-processing of the full matrix of ultrasonic transmit-receive array data for non-destructive evaluation," *NDT Int.*, vol. 38, pp. 701–711, Oct. 2005.
[4] Y. Javadi, C. N. Macleod, S. G. Pierce, A. Gachagan, W. Kerr, J. Ding, S. Williams, M. Vasilev, R. Su, C. Mineo, and J. Dziewierz, "Ultrasonic phased array inspection of wire + arc additive manufacture samples using conventional and total focusing method imaging approaches," *Insight—Non-Destructive Test. Condition Monitor.*, vol. 61, no. 3, pp. 144–148, Mar. 2019.
[5] H. Taheri, "Fast ultrasonic imaging with total focusing method (TFM) for inspection of additively manufactured polymer composite component," in *Proc. 27th ASNT Res. Symp.*, 2018, pp. 212–220.
[6] A. Juengert, "Advanced ultrasonic techniques for nondestructive testing of austenitic and dissimilar welds in nuclear facilities," *AIP Conf. Proc.*, vol. 1949, no. 1, 2018, Art. no. 110002.
[7] D. Romero-Laorden, J. Villazon-Terrazas, O. Martinez-Graullera, A. Ibanez, M. Parrilla, and M. S. Penas, "Analysis of parallel computing strategies to accelerate ultrasound imaging processes," *IEEE Trans. Parallel Distrib. Syst.*, vol. 27, no. 12, pp. 3429–3440, Dec. 2016.
[8] M. Njiki, A. Elouardi, S. Bouaziz, O. Casula, and O. Roy, "A multi-FPGA architecture-based real-time TFM ultrasound imaging," *J. Real-Time Image Process.*, vol. 16, no. 2, pp. 505–521, Apr. 2019.
[9] M. Lewandowski, M. Walczak, B. Witek, J. Rozbicki, and T. Steifer, "A GPU-based portable phased-array system with full-matrix capture," in *Proc. IEEE Int. Ultrason. Symp. (IUS)*, Oct. 2018, pp. 1–3.
[10] C. Wang, J. Mao, T. Leng, Z.-Y. Zhuang, and X.-M. Wang, "Efficient acceleration for total focusing method based on advanced parallel computing in FPGA," *Int. J. Acoust. Vibrat.*, vol. 22, no. 4, pp. 536–540, Dec. 2017.
[11] C. Holmes, B. Drinkwater, and P. Wilcox, "The post-processing of ultrasonic array data using the total focusing method," *Insight—Non-Destructive Test. Condition Monitor.*, vol. 46, no. 11, pp. 677–680, Nov. 2004.
[12] H. Peng, J. Peng, H. Zhu, Z. WANG, and X. GAO, "The efficiency optimization of full matrix capture imaging detection based on increasing the effective aperture," in *Proc. IEEE Far East Forum Nondestruct. Eval./Testing (FENDT)*, Dec. 2014, pp. 6–50.
[13] H. Zhang, Y. Liu, G. Fan, H. Zhang, W. Zhu, and Q. Zhu, "Sparse-TFM imaging of Lamb waves for the near-distance defects in plate-like structures," *Metals*, vol. 9, no. 5, p. 503, Apr. 2019.
[14] H. Hu, J. Du, N. Xu, H. Jeong, and X. Wang, "Ultrasonic sparse-TFM imaging for a two-layer medium using genetic algorithm optimization and effective aperture correction," *NDT Int.*, vol. 90, pp. 24–32, Sep. 2017.
[15] N. Laroche, "Fast inverse approach for the deconvolution of ultrasonic TFM images using a spatially varying PSF in NDT," in *Proc. IEEE Int. Ultrason. Symp. (IUS)*, May 2019, pp. 1985–1988.
[16] H. Zhang, B. Bai, J. Zheng, and Y. Zhou, "Optimal design of sparse array for ultrasonic total focusing method by binary particle swarm optimization," *IEEE Access*, vol. 8, pp. 111945–111953, 2020.

[17] C. E. de C. Kitano, and R. T. Higuti, "Sparse array design using the genetic algorithm for optimizing the radiation pattern of linear Arrays," in *Proc. Brazilian Congr. Biomed. Eng.* Singapore: Springer, 2019, pp. 441–445.

[18] H. Zhang, L. Zeng, G. Fan, H. Zhang, Q. Zhu, and W. Zhu, "Instantaneous phase coherence imaging for near-field defects by ultrasonic phased array inspection," *Sensors*, vol. 20, no. 3, p. 775, Jan. 2020.

[19] M. Sutcliffe, P. Charlton, and M. Weston, "Multiple virtual source aperture imaging for non-destructive testing," *Insight—Non-Destructive Test. Condition Monitor.*, vol. 56, no. 2, pp. 75–81, Feb. 2014.

[20] S. Bannouf, S. Robert, O. Casula, and C. Prada, "Data set reduction for ultrasonic TFM imaging using the effective aperture approach and virtual sources," *J. Phys., Conf. Ser.*, vol. 457, Aug. 2013, Art. no. 012007.

[21] J. H. Holland, "Genetic algorithms and the optimal allocation of trials," *SIAM J. Comput.*, vol. 2, no. 2, pp. 88–105, Jun. 1973.

[22] P. Yang, B. Chen, and S. KR, "A novel method to design sparse linear arrays for ultrasonic phased array," *Ultrasonics*, vol. 44, pp. 717–721, Oct. 2006.

[23] W. SC and Y. Shi, "Optimum beam steering of linear phased arrays," *Wave Motion*, vol. 29, pp. 245–265, Dec. 1999.

[24] M. G. Bray, D. H. Werner, D. W. Boeringer, and D. W. Machuga, "Optimization of thinned aperiodic linear phased arrays using genetic algorithms to reduce grating lobes during scanning," *IEEE Trans. Antennas Propag.*, vol. 50, no. 12, pp. 1732–1742, Dec. 2002.

LIN LUO graduated from the Beijing Institute of Technology, in 1985. He studied with Academician Jiang Wenhan, in 1985. He received the master's and Ph.D. degrees from the Graduate School of the Chinese Academy of Sciences, in 1988 and 2006, respectively.

He is currently a Professor. He was a Visiting Scholar with Tokyo University, Japan, in 2004. His main research directions are high resolution imaging technology, photoelectric image detection of rail transit, and non-destructive image detection of rail transit.

KAI YANG graduated from Southwest Jiaotong University, in 2003. He received the master's and Ph.D. degrees from Southwest Jiaotong University, in 2006 and 2015, respectively.

He is currently a Lecturer. His main research directions are digital image processing and digital signal processing, photoelectric image detection of rail transit, and non-destructive ultrasonic detection of rail transit.

JIN YANG received the bachelor's degree in electronic information science and technology from Southwest Jiaotong University, Chengdu, China, in 2018, where he is currently pursuing the master's degree in optics. His current main research interests are ultrasonic non-destructive testing and related imaging algorithms.

YU ZHANG received the bachelor's degree in engineering in optoelectronics technology and the master's degree in power electronics and electric drive from Southwest Jiaotong University, in 2000 and 2003, respectively. He is currently an Associate Professor. He was a Lecturer, in 2005, and promoted to Associate Professor, in 2010. His main research directions are photoelectric detection and information processing, image processing and three-dimensional measurement, and non-destructive testing technology and its application.

• • •